Proceedings of the Canadian Society for Mechanical Engineering International Congress
32nd Annual Conference of the Computational Fluid Dynamics Society of Canada
Canadian Society of Rheology Symposium
CSME/CFDSC/CSR 2025
May 25–28, 2025, Montréal, Québec, Canada

Microstructural Evolution of Chiral Nematics: A Lid-Driven Cavity Flow Study

Isreal Morawo[1], Dana Grecov[1*]

[1]Department Mechanical Engineering, University of British Columbia, Vancouver BC, Canada
[*]dgrecov@mech.ubc.ca

***Abstract*—**The flow dynamics of cholesteric liquid crystals (CLCs) in a lid-driven cavity (LDC) are investigated using the Landau–de Gennes theory coupled with the Navier-Stokes (NS) equations. The influence of inertia and strong chirality on flow and microstructural evolution is examined by varying the Reynolds number (Re) and chiral strength (Θ). The results show how inertia and chirality interact, leading to different observations, including an increase in the number of defects, striation bending, and a reduction in pitch size. Additionally, velocity fluctuations at different grid points highlight the chaotic nature of the flow, with pronounced and irregular fluctuations at the center of the cavity, indicating strong chaotic dynamics, while more stable fluctuations are observed near the walls. These findings contribute to the understanding of CLC behavior in confined geometries under shear-driven flow.

***Keywords-component*—Cholesteric liquid crystals, lid-driven cavity, inertia, chiral strength, microstructure, numerical simulations.**

I. INTRODUCTION

Cholesteric liquid crystals (CLCs) or *chiral nematics* are a class of liquid crystals (LCs) distinguished by their helical structure, arising from intrinsic chirality [1]. The unique nature of CLCs is defined by two primary structural parameters: the helical pitch. P_0 and the twist sense. Their ability to self-organize into periodic structures makes them essential for applications in photonics, display technologies, and microfluidics. Understanding how CLCs respond to external forces, especially in confined geometries, is critical for optimizing these applications [1]. Despite significant research on CLCs, their microstructural evolution under strong shear-driven flows remains an area of active investigation.

The lid-driven cavity (LDC) problem serves as a classical benchmark in computational fluid dynamics due to its well-defined boundary conditions and ability to show complex flow structures. In the context of CLCs, the LDC provides an ideal setting for examining the interplay between shear forces and CLC microstructure. Notably, how defect migration, striation bending, and pitch variations emerge under strong inertia and chirality remains an open question.

Several studies have explored the behavior of chiral LCs under various conditions. For instance, [2] demonstrated that increasing chiral strength (Θ) enhances striations, reduces pitch, and increases defect formation, while strong viscous effects at high Ericksen numbers (Er) suppress defects. At high Θ, a hexagonal penta-hepta defect structure emerges. Similarly, [3] investigated the role of confinement in determining CNC dispersions (which is a chiral LCs), showing transitions between homeotropic and complex helical configurations. Using the Landau–de Gennes framework, [4] analyzed chiral LC dynamics between cylinders, highlighting the dependence of emergent structures on Deborah number (De). At low De, hexagonal structures dominate, while increasing De leads to their suppression. Additionally, [5] showed that moderate flow conditions facilitate defect relaxation, whereas stronger flows significantly alter defect stability.

In flows involving CLCs, chaotic dynamics often emerge. These dynamics are characterized by irregular and fluctuating velocity fields, which can lead to complex microstructural behavior, including defect formation and migration [2]. The chaotic nature of the flow in CLCs, especially in confined geometries such as the LDC, plays a key role in the formation and evolution of structures within the material. These chaotic fluctuations can result in pronounced variations in the flow's behavior, with regions of intense fluctuation indicating more turbulent or disordered states, while other regions may remain more stable and orderly. Understanding these chaotic dynamics is crucial for predicting the behavior of CLCs under shear-driven flow conditions.

Building upon the numerical framework established in [2], this study investigates the effect of inertia and strong chirality on CLC flow in an LDC. By systematically varying the

4YF/Ambassador Fellowship, NSERC Discovery Grant, WestGrid and the Digital Research Alliance of Canada.

Re and Θ, we examine how these parameters shape defect formation, order parameter variations, microstructural evolution and velocity fluctuation in time. This work advances the understanding of chiral LCs behavior in confined geometries, offering insights relevant to the design and control of CLC-based technologies.

II. Theory and Governing Equation

In the LdG theory, the microstructure and orientation of LCs are described by the second-order tensor $\mathbf{Q}$, known as the tensor order parameter. The $\mathbf{Q}$-tensor field at each spatial point is given by:

$$\mathbf{Q} = S\left(\mathbf{nn} - \frac{1}{3}\mathbf{I}\right) + P\left(\mathbf{mm} - \mathbf{ll}\right), \tag{1}$$

where S is the scalar order parameter, P is the biaxial order parameter, and $\mathbf{n}$, $\mathbf{m}$, and $\mathbf{l}$ are the eigenvectors of $\mathbf{Q}$ corresponding to eigenvalues μ_n, μ_m, and μ_l. The equilibrium scalar order parameter S_{eq} is expressed as:

$$S_{\text{eq}} = 0.25 + 0.75\sqrt{1 - \frac{8}{3}N}, \tag{2}$$

where N is the nematic potential. Alternatively, the $\mathbf{Q}$ tensor can be defined as:

$$\mathbf{Q} = \int \left(\mathbf{bb} - \frac{1}{3}\mathbf{I}\right)\omega d^2\mathbf{b}, \tag{3}$$

where $\mathbf{b}$ is the molecular orientation, $\mathbf{I}$ is an identity matrix, and ω is the orientation distribution function.

For three-dimensional systems, the $\mathbf{Q}$-tensor is defined by the following properties:

$$\mathbf{Q}_{ij} = \mathbf{Q}_{ji} \quad \text{for all} \quad i,j \in \{1,2,3\},$$

and

$$\sum_{i=1}^{3} \mathbf{Q}_{ii} = 0.$$

The dimensionless form of the LdG model for LC flow is given by:

$$\dot{\mathbf{Q}} = F^* + \frac{1}{De}H^*_{\text{sr}} + \frac{1}{Er}H^*_{\text{lr}} + \frac{\Theta}{Er}P^*, \tag{4}$$

where De is the Deborah number, Er is the Ericksen number, P^* is the chiral term, and Θ represents the chiral strength. The chiral term is expressed as:

$$P^* = \epsilon_{mik}\frac{\partial \mathbf{Q}_{mj}}{\partial x_k} + \epsilon_{mjk}\frac{\partial \mathbf{Q}_{mi}}{\partial x_k}, \tag{5}$$

where ϵ_{ijk} is the Levi-Civita symbol, which governs the director twisting patterns. The relevant dimensionless numbers are:

$$De = \frac{U}{6HD_r}, \quad Er = \frac{UHcKT}{6L_1D_r}, \quad \Theta = \frac{L^2}{\zeta^2}, \tag{6}$$

$$R = \frac{Er}{De}, \quad Re = \frac{\rho U^2}{cKT}. \tag{7}$$

Here, U and H represent characteristic velocity and length scales, D_r is rotational diffusivity, c is molecular concentration, K is the Boltzmann constant, T is the absolute temperature, L_1 is the Landau coefficient, ζ is the anisotropic long range length scale, L is the isotropic long range length and ρ is the density. The Θ is inversely related to the helical pitch. Further details on the theory and governing equations can be found in [6].

Equations (8) and (9) represent the dimensionless incompressible continuity equation and the momentum equation of the Navier-Stokes equations written in dimensionless form, respectively:

$$\nabla \cdot \mathbf{u}^* = 0 \tag{8}$$

$$Re\left(\frac{\partial \mathbf{u}^*}{\partial t^*} + (\mathbf{u}^* \cdot \nabla)\mathbf{u}^*\right) = -\nabla p^* + \nabla \cdot \tau_t^* \tag{9}$$

where $\mathbf{u}^*$ is the velocity vector, p^* is the pressure, and τ_t^* is the total stress. Further details on the stress can be found in [6].

III. Numerical Setup

The dimensionless LdG equations, coupled with the Navier–Stokes equations, were solved using COMSOL Multiphysics. The LdG model was implemented in the General Form PDE (g) module, while the momentum equations were solved in the Laminar Flow (spf) module. A Multifrontal Massively Parallel Sparse (MUMPS) solver was used for the coupled system at each time step, with time integration performed using the backward differentiation formula (BDF). The governing equations and numerical setup have been validated in previous studies [2], [4], [6].

A no-slip condition was imposed on all stationary walls, with the top wall driven at a constant velocity. To mitigate corner effects, uniform orientation anchoring was applied: homeotropic anchoring on the top and bottom walls and planar anchoring side as shown in Table 1. The initial conditions for the order parameter tensor Q, were set to zero to ensure an *isotropic state*, while the initial velocity field and pressure (p_0) were also set to zero.

The computational domain consisted of a square cavity of side length $H = 1$ units, as illustrated in Figure 1. Mesh independence was verified by comparing velocity profiles along the center plane, yielding a final mesh of 5,625 elements with an average quality of 1.0 units. Simulations were run for $t = 500$ s to capture the *quasi-stationary* microstructural evolution, consistent with observations in [2], [4], [6]. The molecules of the CLC are represented by an ellipsoid, details can be found in [6]

TABLE. I: Boundary Conditions for Flow Variables

Boundary	U (m/s)	Q	n
Wall I	1	$\left(\frac{-1}{3}, \frac{2}{3}, \frac{-1}{3}\right)$	(0,1)
Other walls	0	$\left(\frac{-1}{3}, \frac{2}{3}, \frac{-1}{3}\right)$	(0,1)

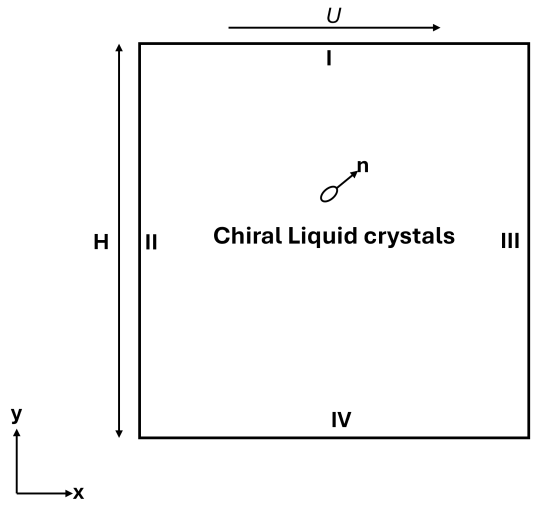

Figure. 1: Lid-driven cavity geometry.

IV. Results and Discussion

This study investigates the effect of inertial and chiral effect on the coupling between flow and microstructural evolution in an LDC flow by varying the Re from 0.01 to 10 and Θ between 70 and 90. While other factors, such as viscous contributions and long-range interactions, are present, the analysis is strictly focused on inertia and chirality. For a detailed discussion on other effects, refer to [6], [7]. To ensure this focus, simulations were performed with an energy ratio of $R = 10^5$ and an Ericksen number of $Er = 100$, where the chosen Er value minimizes viscous effects. The high energy ratio of $R = 10^5$ was specifically selected to enable a clearer evaluation of inertial and chiral influences. For all the simulations the parameters used followed [6]. Selected results from these simulations are presented in the next subsections.

A. Transient Evolution of CLC Structures

Figure 2 presents the molecular visualization of CLC molecules during the transient evolution within the LDC. In this case, the Θ was set to $\Theta = 70$ and the Re to Re $= 0.01$, ensuring a dominant chiral effect while minimizing inertial contributions. To further enhance the chiral influence and suppress viscous effects, Er $= 100$ was used. The CLC molecules were modeled using the method proposed in [2], [4], [6].

At $t = 0$ s (Figure 2a), the system is isotropic as prescribed in the initial condition. However, as time progresses, the chiral nature of the system begins to manifest. By $t = 10$ s (Figure 2b), cholesteric fingerlike structures emerge, these structures continue to evolve, aligning with the imposed shear direction (Figures 2c–2d). By $t = 100$ s, the system reaches a steady state, as no further molecular migrations are observed (Figures 2e–2f). This indicates that the CLC structures have stabilized under the imposed flow conditions.

Figure 3 shows the evolution of streamline patterns. Initially (Figure 3a), the flow is stable and symmetric, but these structures changes over time and become chaotic (Figures 3b–3d), and by $t = 500\,s$ (Figure 3f), the flow remains unsteady with persistent vortex patterns. Summarily, even though the CLC molecules stabilize over time, the streamlines remain unsteady, exhibiting persistent chaotic patterns.

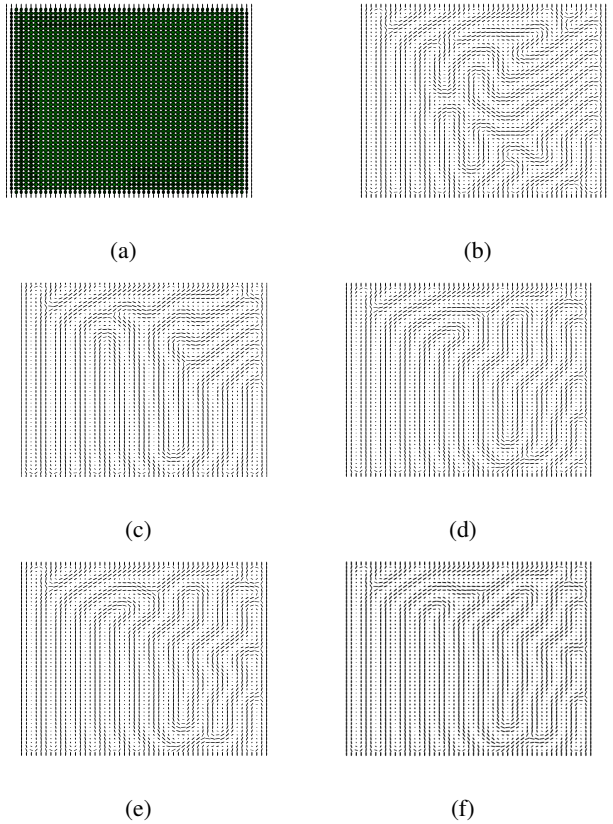

Figure. 2: Molecular visualization at Θ = 70 and Er = 100 at (a) t = 0 s, (b) t = 10 s,(c) t = 20 s, (d) t = 30 s, (e) t = 100 s and (f) t = 500 s.

B. Chiral Effect

Figures 4 and 5 present the visualization of the microstructure and the scalar order parameter (S) at different Θ. At $Re = 0.01$ and $\Theta = 70$ (Figure 4a), defects (low -S regions correspond to defect sites) are primarily concentrated near the boundaries and in the center, with striations distributed throughout the domain. As the $Theta$ increases, the striations bend more, the pitch size decreases, and the number of defects rises (Figure 4b–4c). A similar trend is observed in Figure 5a – 5c at $Re = 10$, where an increase in Θ from 70 to 90 results in a higher defect count.

This increase in defect formation is further illustrated in Figure 6, where the number of defects increases with Θ at $Re = 0.01$. A similar pattern is observed at higher inertia ($Re = 10$), highlighting the role of Θ in defect formation.

Figure 7 and 8 shows the out of plane director contour at different Θ. This helps capture how the molecular orientation of CLCs tilts out of the primary flow plane and provides

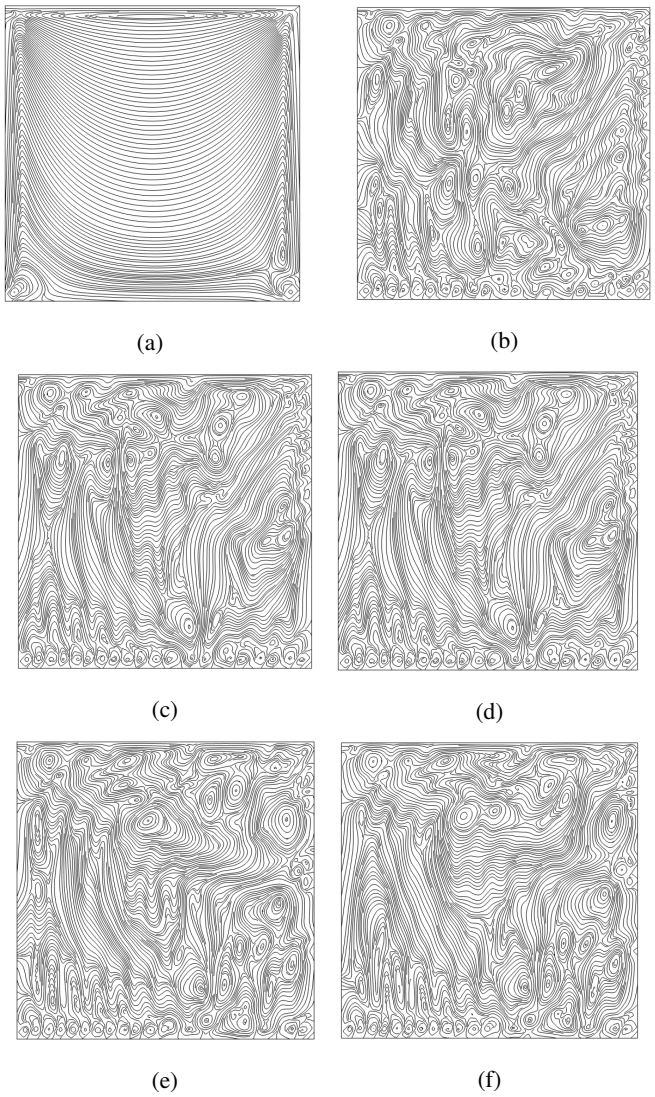

Figure. 3: Streamlines at Θ = 70 and Er = 100 at (a) t = 0 s, (b) t = 10 s, (c) t = 20 s, (d) t = 30 s, (e) t = 100 s and (f) t = 500 s.

a measure of this structural change. The contour transitions from blue to yellow as the director shifts from an in-plane orientation ($|n_z| = 0$) to a fully out-of-plane alignment ($|n_z| = 1$). These regions coincide with the center of the striation lines, highlighting the influence of chiral forces on the system's evolving structure.

Overall, increasing the Θ from 70 to 90 enhances the defect formation, as indicated by the expansion of low-S regions and corresponding $|n_z|$. The migration of defects toward the center of the domain with higher Θ is consistent with previous findings [1], [6].

C. Inertial Effect

- At lower inertia (Figures 4a–4c), the striations bend more prominently at the top in the direction of the flow, emphasizing the weaker effect of inertia and the bending

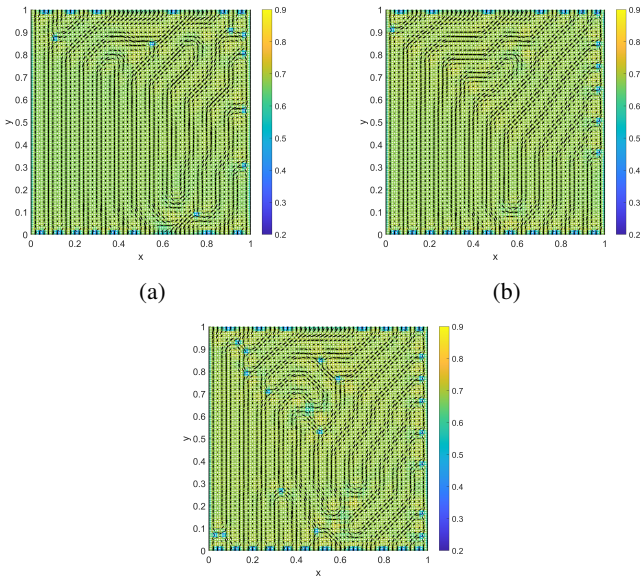

Figure. 4: Microstructure visualizations and scalar order parameter (S) contours at Re = 0.01, Er = 100, t = 500 s: (a) Θ = 70, (b) Θ = 80, (c) Θ = 90. The blue contour shows the defect site.

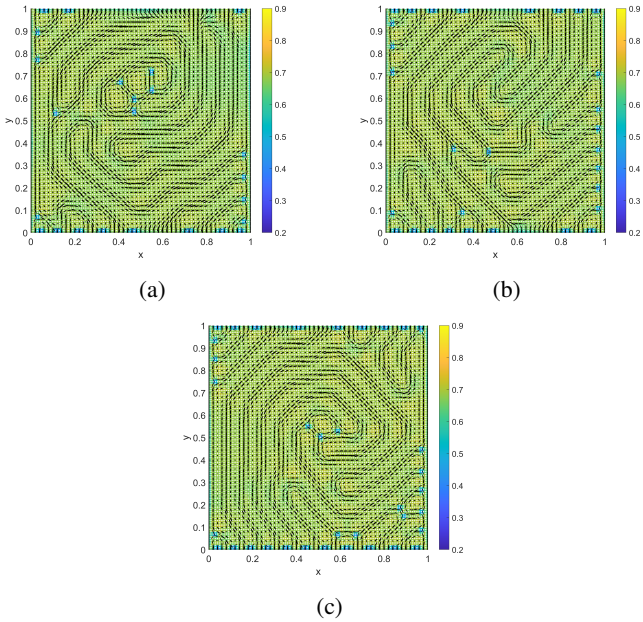

Figure. 5: Microstructure visualizations and scalar order parameter (S) contours at Re = 10, Er = 100, t = 500 s: (a) Θ = 70, (b) Θ = 80, (c) Θ = 90. The blue contour shows the defect site.

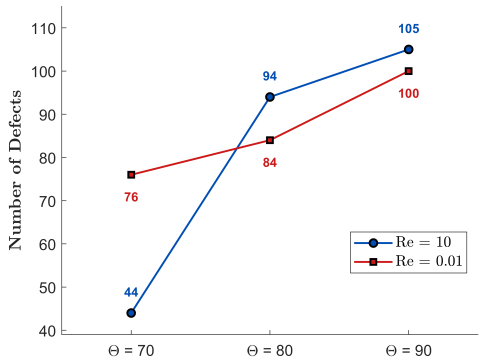

Figure. 6: Number of defects under various (Θ) for $Er = 100$ at $t = 500$ s and different Re.

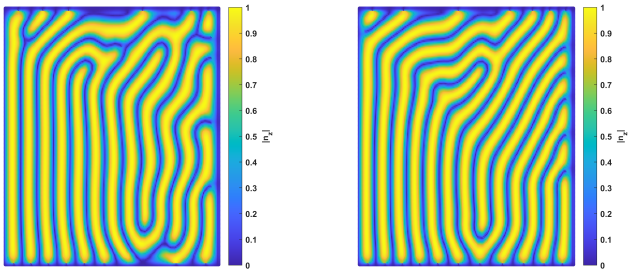

(a) (b)

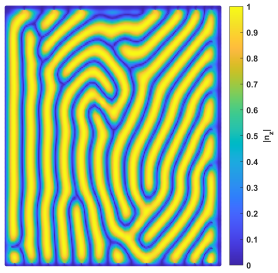

(c)

Figure. 7: Out of plane $|n_z|$ contours at Re = 0.01, Er = 100, t = 500 s: (a) Θ = 70, (b) Θ = 80, (c) Θ = 90.

of cholesteric structures as the Θ increases. Meanwhile, in the left half of the LDC, the striations remain straight. As Re increases (Figures 5a–5c), the striations inside the LDC become more pronouncedly bent, indicating that the flow is increasingly dominated by the inertia effect.

- The increase in the inertia effect (Re = 10) does not necessarily lead to an increase in the number of defects, as shown in Figure 6.
- Another effect of increased inertia, as seen in Figures 4 and 5, is the increase in pitch for the same Θ.
- Figures 7 and 8 also follow this trend, showing that the region with out-of-plane director is larger at higher Re

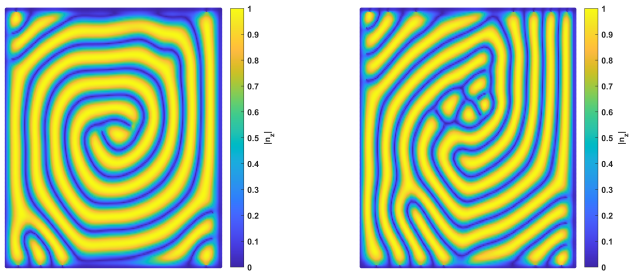

(a) (b)

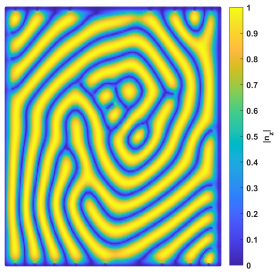

(c)

Figure. 8: Out of plane $|n_z|$ contours at Re = 10, Er = 100, t = 500 s: (a) Θ = 70, (b) Θ = 80, (c) Θ = 90.

compared to lower Re at thesame Θ, further confirming that increasing Re leads to an increase in pitch at the same Θ.

Figure 9 presents the streamline visualization with velocity contours at different Re. At low inertia (Figures 9a–9b), chaotic regions are evident, with small vortices scattered throughout the LDC. As the inertia effect increases (Figures 9c–9d), the flow becomes more structured, with smaller vortices merging into a larger vortex at the center of the LDC, while the corners remain dominated by smaller vortices. This transition leads to a more organized flow structure.

To further explore the chaotic behavior observed in Figure 9a, Figure 10 shows the velocity fluctuations at two points: $(0.5, 0)$ and $(0.5, 0.5)$ within the LDC. At the center of the cavity $(0.5, 0.5)$ (black), the fluctuations are more pronounced and irregular, reflecting strong chaotic dynamics as shown in Figure 10a. In contrast, at the bottom wall $(0.5, 0)$ (blue), the fluctuations are smaller and more stable, suggesting weaker shear effects and the influence of long-range elasticity. Increasing the Re in Figure 10b reduces the fluctuation amplitude by half, but does not eliminate the irregularity at the center. The bottom wall also exhibits reduced fluctuation amplitudes, now smaller than those observed at $Re = 0.01$.

V. Conclusion

This study explores the effects of inertia and Θ on the coupling between flow and microstructural evolution in LDC flow. The findings offer valuable insights.

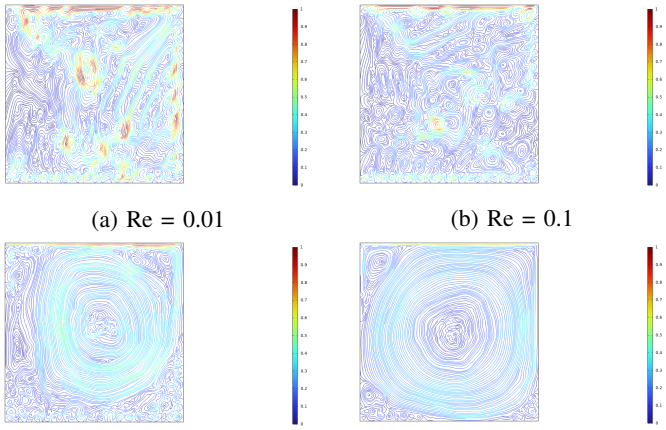

(a) Re = 0.01 (b) Re = 0.1

(c) Re = 1 (d) Re = 10

Figure. 9: Streamlines visualization and velocity contours at Θ = 90, Er = 100, t = 500 s: (a) Re = 0.01, (b) Re = 0.1, (c) Re = 1, (d) Re = 10.

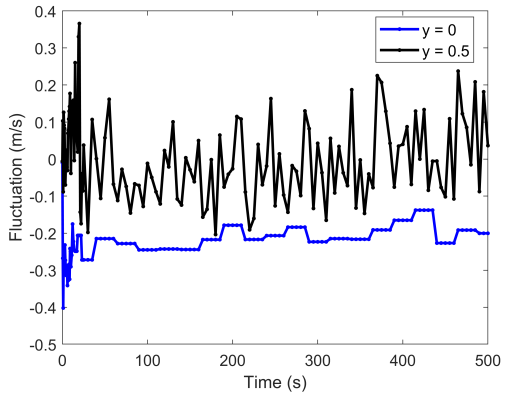

(a)

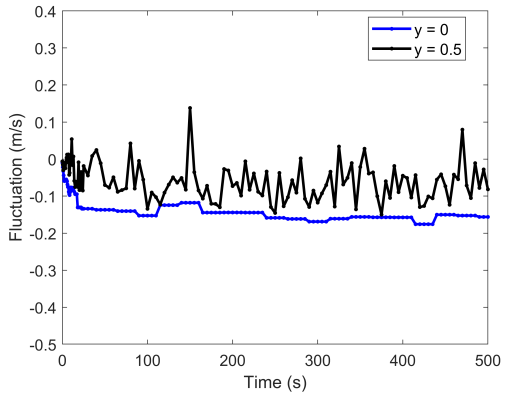

(b)

Figure. 10: Velocity fluctuations at two points $(0.5, 0)$ and $(0.5, 0.5)$ in the LDC, highlighting the transient phase and chaotic dynamics at $\Theta = 90$, Er $= 100$, $t = 500$ s, and (a) Re $= 0.01$ (b) Re $= 10$.

Microstructural evolution, described by using the tensor order parameter **Q** and defect sites identified with the region of low scalar order parameter S, reveals that at $t = 0$ s, the system is isotropic as prescribed in the initial condition. As time progresses, cholesteric fingerlike structures form and align with the shear direction. By $t = 100$ s, the molecules reaches a steady state, with no further molecular migration, indicating stabilization under the given flow conditions. However, in terms of the streamline, the system does not reach a steady state even at $t = 500$ s. Furthermore, increasing Θ reduces the pitch size and increases the number of defects.

As the Re increases, the effect of inertia becomes more pronounced, with striations bending more noticeably, especially at the top of the LDC (Figures 4a–4c, 5a–5c). Despite this, the number of defects does not necessarily increase with higher inertia (Figure 6). Additionally, higher inertia leads to an increase in pitch for the same Θ, as shown in Figures 4,5,7,8. The long-range effects, influenced by boundary conditions, contribute to greater stability along the edges of the system. In these regions, the molecules are constrained by the boundaries, which reduces the degree of fluctuation and instability.

Streamline visualization and velocity contours reveal a transition from chaotic to more structured flow as inertia increases. At low inertia, small vortices dominate the LDC, while higher inertia causes these vortices to merge into a central vortex, leading to a more organized flow structure. The velocity fluctuation plot further characterizes the chaotic dynamics, with pronounced fluctuations at the cavity center, indicating strong chaotic behavior. In contrast, fluctuations near the walls remain more stable, and as Re increases, the fluctuation amplitude behavior at the LDC center diminishes.

In summary, these results highlight the influence of both inertia and Θ on the coupling between flow and microstructural dynamics. Further studies examining additional flow effects in CLCs, along with experimental validation across different flow regimes, are needed to better understand these dynamics.

REFERENCES

[1] Chandrasekhar, S. (1992). Liquid Crystals (2nd ed.). Cambridge University Press.

[2] Li, S., Grecov, D. (2023). Numerical simulation of the 2D lid-driven cavity flow of chiral liquid crystals. Liquid Crystals, 50(5), 798–808. https://doi.org/10.1080/02678292.2023.2179121

[3] Pospisil, M. J., Saha, P., Abdulquddos, S., Noor, M. M., Davis, V. A., Green, M. J. (2018). Orientation relaxation dynamics in cellulose nanocrystal dispersions in the chiral liquid crystalline phase. Langmuir, 34(44), 13274–13282. https://doi.org/10.1021/acs.langmuir.8b02350

[4] Nikzad, A., Grecov, D. (2023). Dynamics of chiral liquid crystals between cylinders using Landau-de Gennes theory. Liquid Crystals, 50(3), 437–452. https://doi.org/10.1080/02678292.2022.2135035

[5] Hernández-Ortiz, J. P., Gettelfinger, B. T., Moreno-Razo, J., de Pablo, J. J. (2011). Modeling flows of confined nematic liquid crystals. Journal of Chemical Physics, 134(13). https://doi.org/10.1063/1.3567098

[6] Morawo, I. I. (2024). Numerical modeling of chiral and achiral liquid crystals in confined geometries. University of British Columbia.

[7] Grecov, D., Rey, A. D. (2002). Theoretical and computational rheology for discotic nematic liquid crystals. Molecular Crystals and Liquid Crystals, 391, 57–94.